Journal of the European Ceramic Society 44 (2024) 284–292

Contents lists available at ScienceDirect

Journal of the European Ceramic Society

journal homepage: www.elsevier.com/locate/jeurceramsoc

Phase evolution and microware dielectric properties of high-entropy spinel-type $(Mg_{0.2}Co_{0.2}Ni_{0.2}Li_{0.4}Zn_{0.2})Al_2O_4$ ceramics

Mingjun Xie [a], Xiao Li [a], Yuanming Lai [a,*], Cong Qi [a], Jun Yin [a], Weiping Gong [b], Yuanxun Li [c], Qian Liu [a], Chongsheng Wu [a]

[a] School of Mechanical and Electrical Engineering, Chengdu University of Technology, Chengdu 610059, China
[b] Guangdong Provincial Key Laboratory of Electronic Functional Materials and Devices, Huizhou University, Huizhou 516001, China
[c] State Key Laboratory of Electronic Thin Films and Integrated Devices, University of Electronic Science and Technology of China, Chengdu 610054, China

ARTICLE INFO

Keywords:
High-entropy ceramics
Phase evolution
Microwave dielectric properties
Single phase
Spinel structure

ABSTRACT

In this study, high-entropy spinel-type $(Mg_{0.2}Co_{0.2}Ni_{0.2}Li_{0.4}Zn_{0.2})Al_2O_4$ ceramics were synthesized by solid-state reaction method. The raw materials gradually formed spinel aluminates from 700 to 1400 °C and finally formed high-entropy $(Mg_{0.2}Co_{0.2}Ni_{0.2}Li_{0.4}Zn_{0.2})Al_2O_4$ ceramics after calcination at 1400 °C for 4 h. The high-configuration entropy and low average atomic-size difference were beneficial to form single-phase high-entropy ceramics. Partial lattice distortion occurred within the high-entropy $(Mg_{0.2}Co_{0.2}Ni_{0.2}Li_{0.4}Zn_{0.2})Al_2O_4$ ceramics structure, and its grain size gradually increased with increasing sintering temperature. The high-entropy $(Mg_{0.2}Co_{0.2}Ni_{0.2}Li_{0.4}Zn_{0.2})Al_2O_4$ ceramics exhibited good microwave dielectric properties when sintered at 1550 °C for 4 h: dielectric constant (ε_r) = 7.4, quality factor (Qf) = 58,200 GHz, and temperature coefficient of resonance frequency (τ_f) = –64 ppm/°C. The ε_r values were mainly affected by the dielectric polarizability. The Qf values were highly related to the relative density and covalency of A-site bond, whereas the τ_f values closely depended on the bond strength of A-site.

1. Introduction

With the rapid development of high-frequency communication systems, the problems such as low signal delay and low dielectric loss of electronic devices are gaining progressively more attention. As one of the essential materials for electronic devices, microwave dielectric ceramics have also attracted significant research attention [1–3]. Noteworthy, a low-dielectric-constant (ε_r below 10) ceramic material with high quality factor (Qf) and near-zero temperature coefficient of resonant frequency (τ_f) is commonly used as high-speed substrate in millimeter-wave communication [4–7]. Low ε_r value can sufficiently reduce the signal propagation delay time [8]. High Qf value can aid in extending the operating frequency ranges of communication systems and play an important role in enhancing frequency selective characteristics and suppressing signal attenuation [9,10]. Moreover, near-zero τ_f value can endow the device with good temperature stability [11]. Therefore, the development of high-performance microwave dielectric ceramics is highly demanded and urgently required.

$MgAl_2O_4$ ceramics with cubic spinel structure have been extensively studied in the microwave dielectric material field [12,13]. The $MgAl_2O_4$ ceramics exhibit a low ε_r value (~8.2); however, a low Qf value (~42, 600 GHz) and large negative τ_f value (–78 ppm/°C) limit their application prospects in the field of millimeter-wave communication [14,15]. Ion substitution is an important strategy to improve the microwave dielectric properties; however, no significant breakthrough can be achieved by conventional ion substitution method. For the excellent performance of high-entropy alloys in the alloys field, the concept of "high-entropy ceramics" has also been proposed [16]. High-entropy ceramics are single-phase ceramics with five or more different cations in equiatomic or near-equiatomic ratios [17,18]. High entropy produces some attractive effects: a high-configuration entropy favors the formation of single-phase solid solutions (high-entropy effect), sluggish kinetics (sluggish diffusion effect), lattice distortions (lattice distortion effect), and a collection of properties that exceeds the characteristics of the constituent materials (cocktail effects) [16,19].

Moreover, the high-configuration entropy of the ceramics is beneficial to improve the simultaneous solubility of multiple components, which provides a new idea and route for improving some properties of

* Corresponding author.
E-mail address: laiyuanming19@cdut.edu.cn (Y. Lai).

https://doi.org/10.1016/j.jeurceramsoc.2023.09.017
Received 13 June 2023; Received in revised form 31 August 2023; Accepted 6 September 2023
Available online 7 September 2023

these materials [19]. In recent years, high-entropy ceramics with excellent microwave dielectric properties have been fabricated and systematically investigated [19–21]. For example, a series of high-entropy perovskite-type $Ba(Zr_{0.2}Ti_{0.2}Sn_{0.2}Hf_{0.2}Me_{0.2})O_3$ (Me = Y^{3+}, Nb^{5+}, Ta^{5+}, V^{5+}, Mo^{6+}, and W^{6+}) ceramics exhibited high temperature stability of dielectric constant from 25 to 200 °C, with low dielectric loss (below 0.002) from 20 Hz to 2 MHz. This result shows that dielectric properties can be tailored via configuration entropy [20]. Moreover, the high-entropy rock salt-type $(Co_{0.2}Cu_{0.2}Mg_{0.2}Ni_{0.2}Zn_{0.2})_{1-x}Li_xO$ oxides exhibited a large relative dielectric constant (above 1000) over a wide frequency range (100 Hz–2.3 MHz) and the dielectric loss was found to be less than 0.01 when the frequency was below 1 MHz [21]. Besides, the high-entropy olivine-type $Li(Gd_{0.2}Ho_{0.2}Er_{0.2}Yb_{0.2}Lu_{0.2})GeO_4$ ceramics exhibited outstanding microwave dielectric properties with a near-zero τ_f of –3 ppm/°C [19]. Therefore, it is expected that high entropy can improve the microwave dielectric properties of spinel aluminate ceramics.

In this study, the microwave dielectric properties of $MgAl_2O_4$ ceramics were improved by synthesizing high-entropy $(Mg_{0.2}Co_{0.2}Ni_{0.2}Li_{0.4}Zn_{0.2})Al_2O_4$ ceramics via solid-state reaction. Furthermore, there were significant differences in configuration entropy and average atomic-size difference between the high-entropy $(Mg_{0.2}Co_{0.2}La_{0.2}Li_{0.2}Zn_{0.2})Al_2O_4$ and $(Mg_{0.2}Co_{0.2}Ni_{0.2}Li_{0.4}Zn_{0.2})Al_2O_4$ ceramics. Therefore, to investigate the forming ability of single-phase high-entropy ceramics, the $(Mg_{0.2}Co_{0.2}La_{0.2}Li_{0.2}Zn_{0.2})Al_2O_4$ with equal proportions of A-site was used as a control sample. The phase evolution of high-entropy $(Mg_{0.2}Co_{0.2}Ni_{0.2}Li_{0.4}Zn_{0.2})Al_2O_4$ ceramics was systematically investigated. Finally, the phase compositions, microstructures, and microwave dielectric properties of high-entropy $(Mg_{0.2}Co_{0.2}Ni_{0.2}Li_{0.4}Zn_{0.2})Al_2O_4$ and $(Mg_{0.2}Co_{0.2}La_{0.2}Li_{0.2}Zn_{0.2})Al_2O_4$ ceramics were characterized and explored.

2. Experimental procedure

High-entropy $(Mg_{0.2}Co_{0.2}Ni_{0.2}Li_{0.4}Zn_{0.2})Al_2O_4$ and $(Mg_{0.2}Co_{0.2}La_{0.2}Li_{0.2}Zn_{0.2})Al_2O_4$ ceramics were synthesized by the solid-state reaction method. The analytically pure raw materials MgO, La_2O_3, $CoCO_3$, $NiCO_3$, Li_2CO_3, ZnO, and Al_2O_3 were obtained from Shanghai Macklin Biochemical Co. Ltd and weighed according to the stoichiometric ratios in $(Mg_{0.2}Co_{0.2}Ni_{0.2}Li_{0.4}Zn_{0.2})Al_2O_4$ and $(Mg_{0.2}Co_{0.2}La_{0.2}Li_{0.2}Zn_{0.2})Al_2O_4$. The weighed powders were ball milled with yttrium-stabilized zirconia balls in deionized water for 4 h, and mixed slurry was dried at 100 °C. Then, the mix powders of $(Mg_{0.2}Co_{0.2}Ni_{0.2}Li_{0.4}Zn_{0.2})Al_2O_4$ and $(Mg_{0.2}Co_{0.2}La_{0.2}Li_{0.2}Zn_{0.2})Al_2O_4$ were dried and calcined at 1400 and 1350 °C for 4 h, respectively. The calcined powders were again ball-milled and dried. Then, the calcined powders were mixed with polyvinyl alcohol (PVA, 10 wt%) solution, and pressed into cylinders with a diameter of 12 mm and a thickness of 6 mm under a pressure of 20 MPa. Next, the $(Mg_{0.2}Co_{0.2}Ni_{0.2}Li_{0.4}Zn_{0.2})Al_2O_4$ and $(Mg_{0.2}Co_{0.2}La_{0.2}Li_{0.2}Zn_{0.2})Al_2O_4$ pellets were heated from room temperature to 1000 °C at the rate of 10 °C/min and held at 600 °C for 4 h to eliminate PVA. Subsequently, the pellets were further heated to the sintering temperature (1500–1600 °C and 1450–1600 °C, respectively) at the rate of 5 °C/min and sintered for 4 h. Finally, it was dropped to 500 °C at the rate of 5 °C/min and allowed to cool down to room temperature naturally.

The relative density ($\rho_{relative}$) of samples was measured at room temperature by Archimedes' method (see Supplementary Information). The crystalline phase was analyzed by powder X-ray diffraction (XRD, Miniflex 600, Rigaku, Japan) with 2θ ranging from 10° to 120° and a step of 0.02° at room temperature with CuK_α radiation. The detailed structure was obtained by refinements by using the Fullprof program [22]. The selected area electron diffraction (SAED) patterns and high-resolution transmission electron microscopy (HRTEM, JEM-2100 Electron Microscope) images were obtained at a working voltage of 200 kV. The phase evolution of the samples was investigated by thermogravimetry-differential scanning calorimetry (TG-DSC) using a simultaneous thermal analyzer (Model NETZSCH STA 449F5). The investigation was carried out at a heating rate of 10 K/min in static air from 30 to 1400 °C and by in-situ XRD (Model X'Pert Pro, PANalytical) in the temperature range of 25–1400 °C. The morphology of the polished and thermally etched surface of the samples was characterized by scanning electron microscopy (SEM; JSM-6490, JEOL, Japan) at an accelerating voltage of 15 kV. The thermal etching process was carried out at a temperature 150 °C lower than the sintering temperature for 4 h. The compositions of samples were analyzed by energy dispersive X-ray spectroscopy (EDS). The microwave dielectric properties of each sample were measured by the Hakki–Coleman dielectric resonator cavity method. The τ_f (ppm/°C) value was calculated by using the following equation [15]:

$$\tau_f = \frac{f(85°C) - f(25°C)}{(85-25) \times f(25°C)} \times 10^6 \quad (1)$$

where f(85 °C) and f(25 °C) represent the resonant frequency at 85 °C and 25 °C, respectively.

3. Results and discussion

The bulk density of the high-entropy $(Mg_{0.2}Co_{0.2}Ni_{0.2}Li_{0.4}Zn_{0.2})Al_2O_4$ ceramics increases from 3.60 to 3.83 g/cm^3 with the increase in the temperature from 1500 to 1550 °C, corresponding to an increase in the relative density from 88.33 % to 94.04 %. With the further increase in the sintering temperature, both the bulk density and relative density show an overall decreasing trend (see Fig. S1 in Supplementary Information). Fig. 1 shows the XRD patterns of high-entropy $(Mg_{0.2}Co_{0.2}Ni_{0.2}Li_{0.4}Zn_{0.2})Al_2O_4$ and $(Mg_{0.2}Co_{0.2}La_{0.2}Li_{0.2}Zn_{0.2})Al_2O_4$ ceramics sintered at different temperatures. The XRD patterns of high-entropy $(Mg_{0.2}Co_{0.2}Ni_{0.2}Li_{0.4}Zn_{0.2})Al_2O_4$ ceramics can be indexed to the PDF No. #75–1799 of the spinel structure $MgAl_2O_4$ with Fd-3 m space group. However, besides spinel-type $MgAl_2O_4$ phase, a secondary phase of $LaAlO_3$ (PDF #76–2373) was also observed in $(Mg_{0.2}Co_{0.2}La_{0.2}Li_{0.2}Zn_{0.2})Al_2O_4$ ceramics (see Fig. 1(b)).

The configuration entropy (ΔS_{config}) and average atomic-size difference (δ) are considered as the main factors for the formation of single-phase high-entropy ceramics (the calculated results are listed in Supplementary Information Table S1) [23,24]. The ΔS_{config} value of high-entropy $(Mg_{0.2}Co_{0.2}Ni_{0.2}Li_{0.4}Zn_{0.2})Al_2O_4$ ceramics (1.65R) is larger than that of $(Mg_{0.2}Co_{0.2}La_{0.2}Li_{0.2}Zn_{0.2})Al_2O_4$ ceramics (1.61R). Owing to the high temperature and the value of ΔS_{config} being larger than 1.5R, the product of absolute temperature and ΔS_{config} can overcome the enthalpy of the mixture, which makes the Gibbs free energy negative to produce a single-phase high-entropy ceramic [23]. Moreover, a necessary criterion for the formation of a single-phase high-entropy alloy is that the δ value of the solid solution should be sufficiently small (δ below 4 %) [24]. Practically, the δ value of high-entropy $(Mg_{0.2}Co_{0.2}Ni_{0.2}Li_{0.4}Zn_{0.2})Al_2O_4$ ceramics (3.31 %) was found to be smaller than that of $(Mg_{0.2}Co_{0.2}La_{0.2}Li_{0.2}Zn_{0.2})Al_2O_4$ ceramics (14.64 %), and a solid solution was formed. Therefore, high-configuration entropy and relatively low average atomic-size difference are beneficial to form a single-phase high-entropy ceramic material.

For the further systematic investigation of the phase compositions and crystal structures of high-entropy $(Mg_{0.2}Co_{0.2}Ni_{0.2}Li_{0.4}Zn_{0.2})Al_2O_4$ and $(Mg_{0.2}Co_{0.2}La_{0.2}Li_{0.2}Zn_{0.2})Al_2O_4$ ceramics, the XRD data were refined by using the Fullprof program. The refined patterns of the high-entropy ceramics sintered at 1550 °C are shown in Fig. 2 (other refined XRD patterns are exhibited in Figs. S2 and S3 in the Supplementary Information), and the Rietveld refinement results are listed in Tables S2 and S3 in the Supplementary Information. All the fitted curves agree well with the experimental data, and the positions of the Bragg reflections are consistent with the indexed peaks. This result indicates that the phase compositions obtained by XRD analysis are reasonable.

The SEM images of thermal-etched surfaces for high-entropy

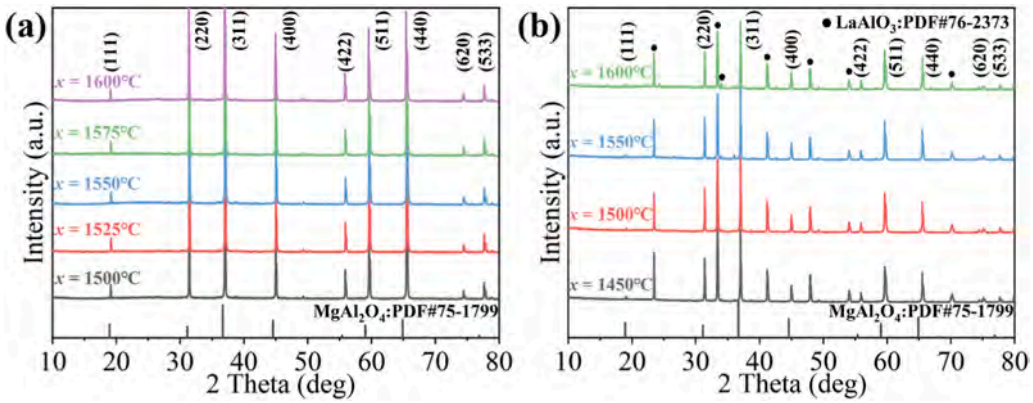

Fig. 1. XRD patterns of the high-entropy ceramics sintered at different temperatures. (a) High-entropy $(Mg_{0.2}Co_{0.2}Ni_{0.2}Li_{0.4}Zn_{0.2})Al_2O_4$ ceramics sintered at 1500–1600 °C; (b) High-entropy $(Mg_{0.2}Co_{0.2}La_{0.2}Li_{0.2}Zn_{0.2})Al_2O_4$ ceramics sintered at 1450–1600 °C.

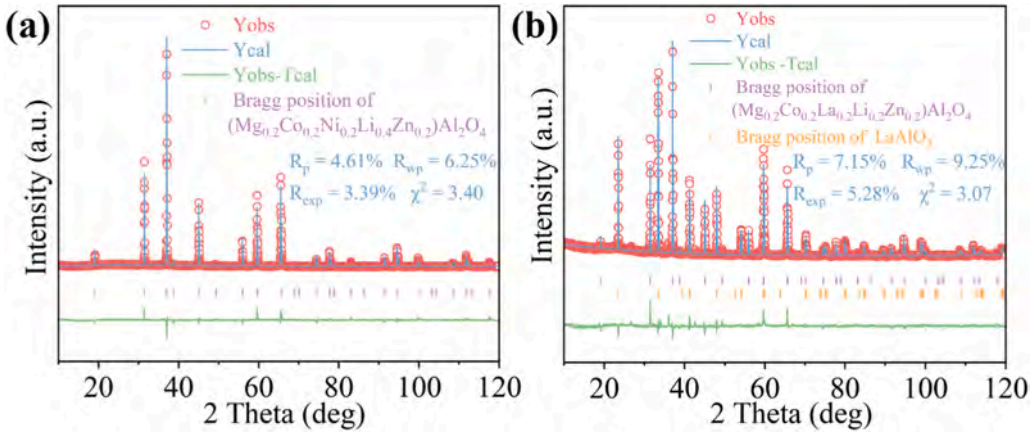

Fig. 2. Rietveld refinements of XRD patterns for the high-entropy ceramics sintered at 1550 °C. (a) High-entropy $(Mg_{0.2}Co_{0.2}Ni_{0.2}Li_{0.4}Zn_{0.2})Al_2O_4$ ceramics; (b) High-entropy $(Mg_{0.2}Co_{0.2}La_{0.2}Li_{0.2}Zn_{0.2})Al_2O_4$ ceramics.

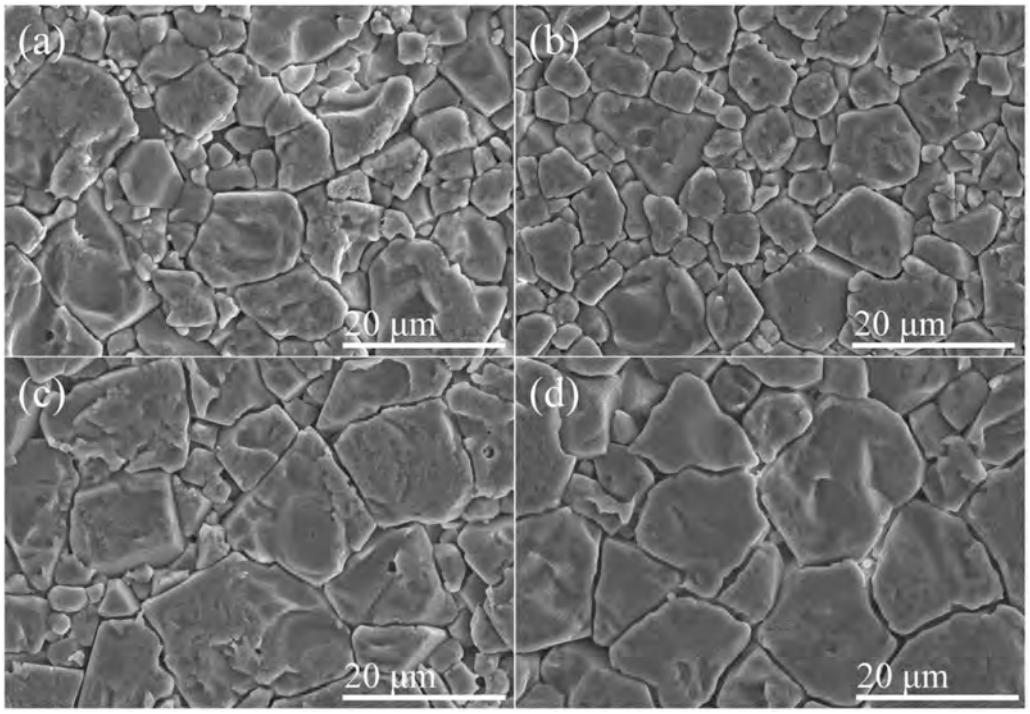

Fig. 3. The SEM images of high-entropy $(Mg_{0.2}Co_{0.2}Ni_{0.2}Li_{0.4}Zn_{0.2})Al_2O_4$ ceramics: (a) 1525 °C; (b) 1550 °C; (c) 1575 °C; (d) 1600 °C.

$(Mg_{0.2}Co_{0.2}Ni_{0.2}Li_{0.4}Zn_{0.2})Al_2O_4$ ceramics are displayed in Fig. 3. The average grain size gradually increased with the increase of sintering temperature, which indicates that high sintering temperature can promote the grain growth of high-entropy $(Mg_{0.2}Co_{0.2}Ni_{0.2}Li_{0.4}Zn_{0.2})Al_2O_4$ ceramics (see Fig. 3(a)–(d)). Fig. 3(a) presents an anomalous grain growth and inhomogeneous grain distribution, corresponding to low relative density. Moreover, the microstructure of the samples sintered at 1550 and 1600 °C are well crystallized and present a uniform grain distribution (see Fig. 3(b) and (d)), corresponding to high relative density. Furthermore, Fig. 3(c) shows the presence of significant pores, which induce the reduction of relative density. The microstructural evolution was attributed to the combined effects of lattice and grain boundary diffusion, which led to elemental homogenization and densification [25]. Moreover, the volatile diffusion of Li^+ at high temperatures forms surface regions with enhanced diffusion along grain boundaries, which can promote grain growth and microstructure densification [26,27].

In order to verify the phase composition of high-entropy $(Mg_{0.2}Co_{0.2}La_{0.2}Li_{0.2}Zn_{0.2})Al_2O_4$ ceramics, the corresponding SEM and EDS analyses were carried out (see Figs. S4 and S5 in Supplementary Information). The results show that the light-colored blocky morphology mainly corresponds to the secondary phase $LaAlO_3$. Furthermore, in order to investigate the distribution of elements and further verify the composition of high-entropy $(Mg_{0.2}Co_{0.2}Ni_{0.2}Li_{0.4}Zn_{0.2})Al_2O_4$ ceramics, the EDS mapping was performed (see Fig. S6 in Supplementary Information). The results demonstrate that all elements (Al, Zn, Mg, Co, and Ni) were homogeneously distributed without any segregation (Li cannot be accepted detected by EDS). The A-site element contents could be considered close to the equimolar ratio, and the ratio of A-site elements, Al, and O was found to be consistent with the stoichiometry of AB_2O_4.

Fig. 4(a) shows the HRTEM image of high-entropy $(Mg_{0.2}Co_{0.2}Ni_{0.2}Li_{0.4}Zn_{0.2})Al_2O_4$ ceramics sintered at 1550 °C for 4 h. HRTEM image reveals excellent crystallinity and sharp lattice fringes. The structural model of high-entropy $(Mg_{0.2}Co_{0.2}Ni_{0.2}Li_{0.4}Zn_{0.2})Al_2O_4$ ceramics, which was obtained from XRD refinements, was embedded in HRTEM image along the direction of the $[04\bar{4}]$ zone axis (Fig. 4(a)). This further confirms that high-entropy $(Mg_{0.2}Co_{0.2}Ni_{0.2}Li_{0.4}Zn_{0.2})Al_2O_4$ ceramics form a spinel-type single phase. Furthermore, the SAED patterns of high-entropy $(Mg_{0.2}Co_{0.2}Ni_{0.2}Li_{0.4}Zn_{0.2})Al_2O_4$ ceramics are shown in Fig. 4(b). The clean, bright, and sharp diffraction spots also indicate the formation of high-entropy $(Mg_{0.2}Co_{0.2}Ni_{0.2}Li_{0.4}Zn_{0.2})Al_2O_4$ ceramics with a spinel structure having Fd-3 m space group.

Fig. 5 shows the HRTEM image of high-entropy $(Mg_{0.2}Co_{0.2}Ni_{0.2}Li_{0.4}Zn_{0.2})Al_2O_4$ ceramics sintered at 1550 °C for 4 h. Fig. 5(a) presents that the FFT (Fourier transform map) pattern along the $[\bar{2}24]$ zone axis of the blue square frame region was obtained to reflect the single-crystal characteristic of high-entropy $(Mg_{0.2}Co_{0.2}Ni_{0.2}Li_{0.4}Zn_{0.2})Al_2O_4$ ceramics, which exhibit a significant spinel structure. Furthermore, the HRTEM images of high-entropy $(Mg_{0.2}Co_{0.2}Ni_{0.2}Li_{0.4}Zn_{0.2})Al_2O_4$ ceramics presented in Fig. 5(b) and (c) show that the measured interplanar spacing is 0.243 and 0.288 nm, respectively. Both the values match well with the theoretical values: 0.244 nm of (311) and 0.287 nm of (220) from PDF No. #75–1799, as well as they are in well agreement with the XRD results. Moreover, Fig. 5(d) shows some edge dislocations marked by the yellow "T" symbol in grains, which indicates the existence of lattice distortion within high-entropy $(Mg_{0.2}Co_{0.2}Ni_{0.2}Li_{0.4}Zn_{0.2})Al_2O_4$ ceramics caused by the A-site atomic size difference. Compared to Fig. 5 (d), Fig. 5(e) shows neatly arranged and uniform lattice fringes, which indicates the occurrence of only partial lattice distortion within high-entropy $(Mg_{0.2}Co_{0.2}Ni_{0.2}Li_{0.4}Zn_{0.2})Al_2O_4$ ceramics.

In order to further analyze the phase evolution process of high-entropy $(Mg_{0.2}Co_{0.2}Ni_{0.2}Li_{0.4}Zn_{0.2})Al_2O_4$ ceramics, the TG-DSC and in-situ XRD studies were implemented. Fig. 6(a) illustrates that a weight loss of about 6.3 % was observed in TG curve below 200 °C, corresponding to the first endothermic peak in DSC curve at 138 °C. This is primarily due to the evaporation of residual water and the formation of trace amounts of basic zinc carbonate [28,29]. Furthermore, a large weight loss of about 13 % occurred in the temperature range of 200–700 °C, which is related to the decomposition of raw materials $CoCO_3$ and $NiCO_3$ to CoO, NiO, and CO_2 at about 500 °C [30–32]. The DSC curve indicates the temperature of 700 °C to be an important transition temperature, inferring that the reaction started at about 700 °C. Moreover, a weight loss of about 2.9 % was observed in the TG curve, corresponding to the exothermic peak in DSC curve at 720 °C. This result is attributed to the reaction of CoO and NiO with Al_2O_3 to form spinel aluminates. Moreover, raw material Li_2CO_3 decomposed into Li_2O and CO_2 relatively slowly, which can be attributed to the inhibition of the decomposition of Li_2CO_3 by the high pressure of CO_2 [33]. Further, Li_2O tended to absorb CO_2 during the decomposition reaction at moderate temperature or pressure, which also hindered the escape of CO_2 gas [34–36].

Two exothermic peaks are also observed at 1250 and 1368 °C in the DSC curve. These peaks are attributed to the reaction of raw materials ZnO and Al_2O_3 forming spinel $ZnAl_2O_4$ at about 900–1400 °C [37–39], and the reaction between raw materials MgO and Al_2O_3 forming spinel $MgAl_2O_4$ at about 1200–1400 °C [40–42]. Moreover, Fig. 6(b) also shows that the intensity of the diffraction peak at 36.09° corresponding to the ZnO (101) plane gradually decreased with increasing temperature. However, the intensity of the diffraction peak at 36.73° corresponding to $MgAl_2O_4$ (311) plane gradually increased, and all the in-situ

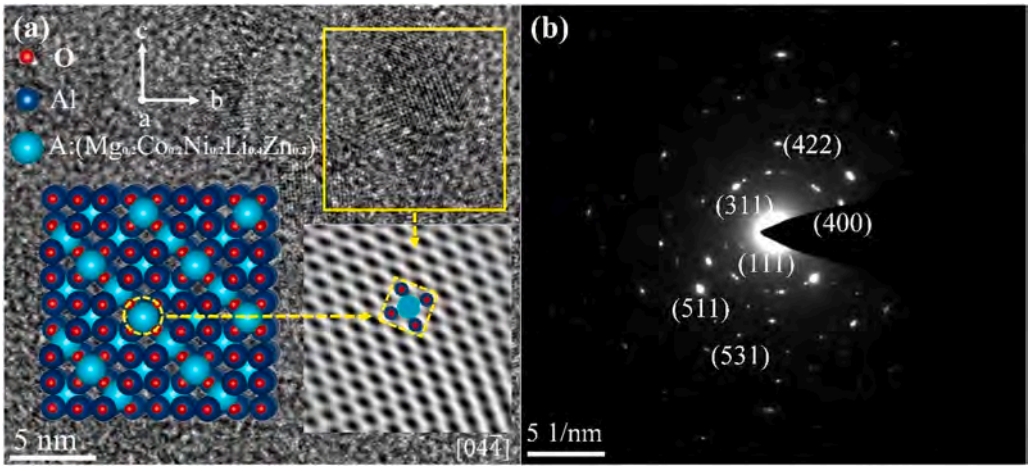

Fig. 4. The crystal structure, HRTEM image, and SAED patterns of high-entropy $(Mg_{0.2}Co_{0.2}Ni_{0.2}Li_{0.4}Zn_{0.2})Al_2O_4$ ceramics. (a) The crystal structure and HRTEM image viewed along the $[04\bar{4}]$ zone axis; (b) The SAED patterns.

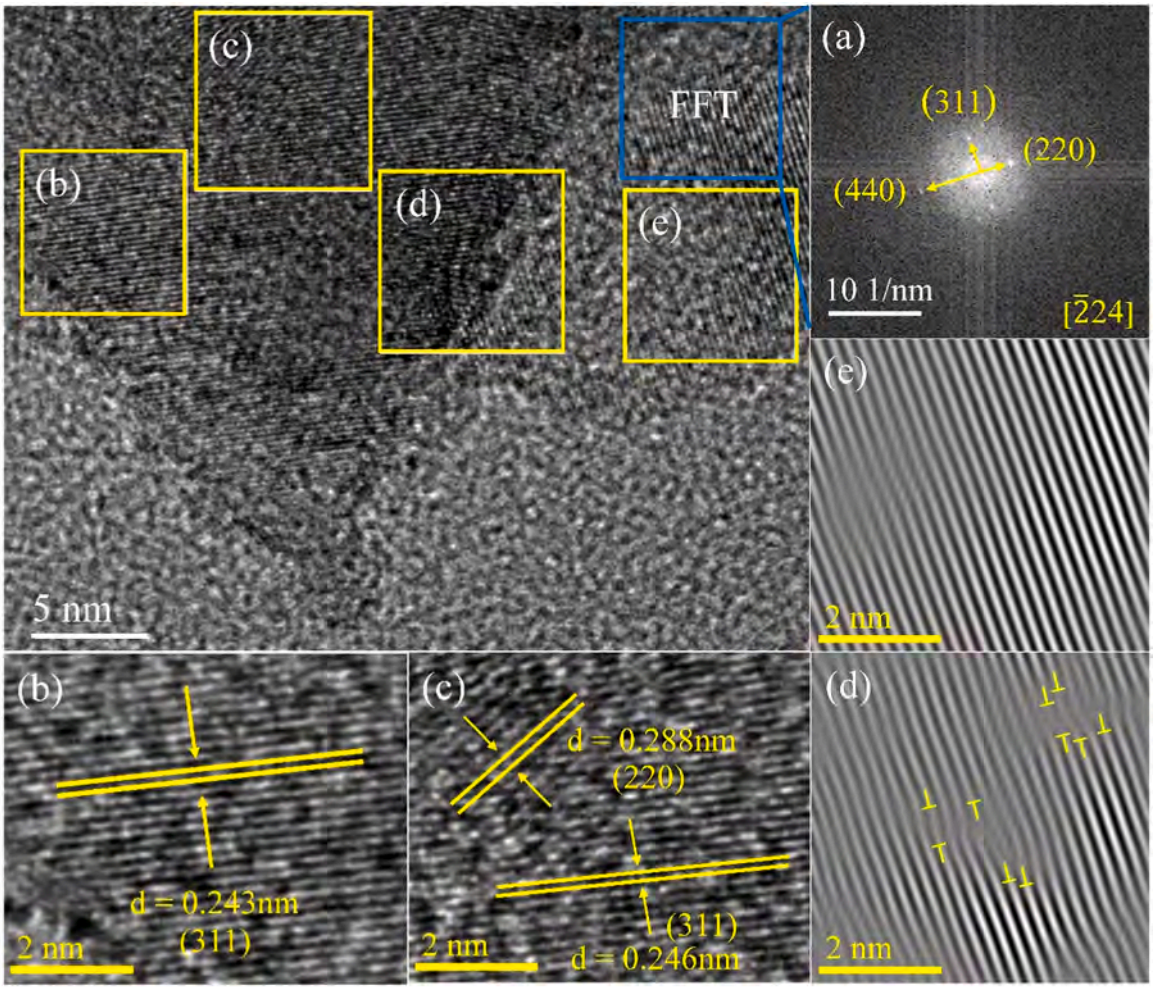

Fig. 5. The HRTEM images of high-entropy $(Mg_{0.2}Co_{0.2}Ni_{0.2}Li_{0.4}Zn_{0.2})Al_2O_4$ ceramics. (a) FFT image viewed along the [$\bar{2}$24] zone axis; (b) and (c) Enlarged images from the regions in the HRTEM image; (d) and (e) Enlarged IFFT images from the regions in the HRTEM image.

XRD patterns tended to be close to the XRD pattern of $MgAl_2O_4$. Moreover, the presence of a small amount of ZnO and Li_2CO_3 was observed in the samples at 1400 °C, as indicated by the in-situ XRD data obtained at 1400 °C for 10 min. The formation of $ZnAl_2O_4$ is a reaction process in which Zn^{2+} undergo gradual diffusion to Al_2O_3 [43,44]. The reaction between the raw materials does not get complete due to the short reaction time, which is a kinetically driven reaction [45]. Furthermore, the XRD pattern of the samples calcined at 1400 °C for 4 h is shown in Fig. 6 (b), which is in good agreement with the PDF No. #75–1799 of $MgAl_2O_4$. Notably, all raw materials gradually formed the high-entropy $(Mg_{0.2}Co_{0.2}Ni_{0.2}Li_{0.4}Zn_{0.2})Al_2O_4$ ceramics. The reaction process is indicated in the following equation:

$$(Ni, Co, Mg, Zn)Al_2O_4(s) + Li_2O(s) + Al_2O_3(s) \rightarrow (Mg_{0.2}Co_{0.2}Ni_{0.2}Li_{0.4}Zn_{0.2})Al_2O_4(s) \quad (2)$$

Fig. 7(a) shows the ε_r values of the high-entropy $(Mg_{0.2}Co_{0.2}Ni_{0.2}Li_{0.4}Zn_{0.2})Al_2O_4$ ceramics sintered at 1500–1600 °C. In order to further analyze the ε_r values of high-entropy $(Mg_{0.2}Co_{0.2}Ni_{0.2}Li_{0.4}Zn_{0.2})Al_2O_4$ ceramics, the Clausius–Mosotti equation could be used to estimate the ε_{theo} of the ceramics [46]:

$$\varepsilon_{theo} = \frac{3V_m + 8\pi\alpha_D}{3V_m - 4\pi\alpha_D} \quad (3)$$

where α_D and V_m denote the dielectric polarizability and the molar volume, respectively. The α_D could be calculated by using the Shannon additive rule [46]:

$$\alpha((Mg_{0.2}Co_{0.2}Ni_{0.2}Li_{0.4}Zn_{0.2})Al_2O_4) = 0.2 \times (\alpha_{Mg^{2+}} + \alpha_{Co^{2+}} + \alpha_{Ni^{2+}} + \alpha_{Zn^{2+}}) + 0.4 \times \alpha_{Li^+} + 4 \times \alpha_{O^{2-}} + 2 \times \alpha_{Al^{3+}} \quad (4)$$

where the ionic polarizabilities of Mg^{2+}, Co^{2+}, Ni^{2+}, Li^+, Zn^{2+}, Al^{3+}, and O^{2-} are 1.32, 1.65, 1.23, 1.20, 0.79, 1.32, and 2.01 Å^3, respectively [46]. The α_D value is 11.348 Å^3. Porosity is also an important factor affecting the ε_r value. The porosity-corrected dielectric constant (ε_{rc}) was calculated by using the following equation [47]:

$$\varepsilon_r = \varepsilon_{rc}\left(1 - \frac{3p(\varepsilon_{rc} - 1)}{2\varepsilon_{rc} + 1}\right) \quad (5)$$

where ε_r and $p = (1-\rho_{relative})$ are the measured dielectric constant and porosity, respectively (see Table S4 in Supplementary Information). Fig. 7(a) shows that the variation tendency of ε_r values is consistent with that of ε_{rc} values. The ε_{rc} values deviate from the ε_{theo} values (~8.95), which may be caused by the rattling effect. The rattling causes the tilting of the B cation–anion bond from an octahedron to a neighboring octahedron in an opposite direction, thus doubling up the repeat distances perpendicular to the tilt axis [48]. Furthermore, if the B cation–anion bond distance is maintained, the B cation–B cation distance (bond length) becomes shorter and thus influences the bond strength. Moreover, rattling effect and B-site bond valence are a function of bond strength [49]. An increase in the Al–O bond valence indicates that the Al–O bond length becomes shorter, and the ionic polarizability becomes

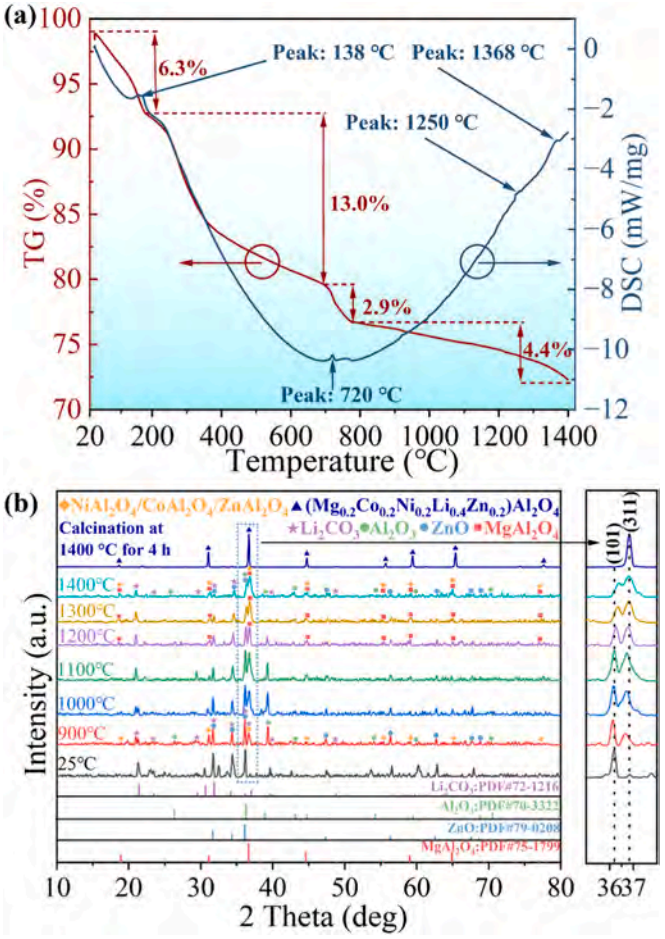

Fig. 6. The TG-DSC curves and in-situ XRD patterns of high-entropy $(Mg_{0.2}Co_{0.2}Ni_{0.2}Li_{0.4}Zn_{0.2})Al_2O_4$ ceramics. (a) The TG-DSC curves; (b) The in-situ XRD patterns.

weak [50]. Therefore, the change in the bond valence of the B-site leads to a deviation between ε_{rc} and ε_{theo}. The samples sintered at 1550 °C exhibited low dielectric constants due to the increase of the B-site bond valence, resulting in the increase of rattling effect (see Table S5 in Supplementary Information).

Fig. 7(b) displays the deviation value of ε_{theo} and ε_r. The positive deviation reveals that the ε_r value is smaller than the ε_{theo} value. The variation trend of deviation value is the same as that of the relative density, indicating that the dielectric constant is determined by ionic polarization and densification [51]. Comparative analysis indicates that high-entropy $(Mg_{0.2}Co_{0.2}La_{0.2}Li_{0.2}Zn_{0.2})Al_2O_4$ ceramics exhibited large ε_r values (~9.5, see Fig. S7 in Supplementary Information). This can be attributed to the fact that the secondary phase $LaAlO_3$ possessed a large ε_r value (~24.0) [52]. Furthermore, compared to $MgAl_2O_4$ ceramics (~8.2), high-entropy $(Mg_{0.2}Co_{0.2}Ni_{0.2}Li_{0.4}Zn_{0.2})Al_2O_4$ ceramics exhibited a lower ε_r value (~7.4).

Fig. 7(c) shows the Qf values of the high-entropy $(Mg_{0.2}Co_{0.2}Ni_{0.2}Li_{0.4}Zn_{0.2})Al_2O_4$ ceramics sintered at 1500–1600 °C. In general, the Qf values are dominated by two factors; namely, the intrinsic factors that are mainly dominated by the bond characteristics, cation disorders, and lattice vibration. In contrast, the extrinsic factors are generally dominated by densification, secondary phase, and grain boundaries [14,53]. For comprehensive evaluation of the bond characteristics of $(Mg_{0.2}Co_{0.2}Ni_{0.2}Li_{0.4}Zn_{0.2})Al_2O_4$ samples, the relationship between the bond strength (s) and the covalency (fc) between cations and oxygen ions can be used to calculate the covalency of A-site bond in tetrahedron, which can be calculated by using the following rule formula [54–57]:

$$s = \left(\frac{R_{avg}}{R}\right)^{-N} \tag{6}$$

$$f_c = a \cdot s^M \tag{7}$$

$$\text{the degree of covalency}(\%) = \left(\frac{f_c}{s}\right) \times 100\% \tag{8}$$

where R_{avg} is the average bond length between the cation and oxygen ion. R and N denote the empirical constants that depend on the cation site. Moreover, a and M are empirical constants that depend on the number of electrons (see Table S6 in Supplementary Information). Fig. 7 (c) illustrates that the variation trend of the Qf values is similar to that of the covalency of A-site bond (1525–1600 °C) and highly consistent with the relative density (1500–1600 °C). Fig. 3 shows the SEM images of the high-entropy $(Mg_{0.2}Co_{0.2}Ni_{0.2}Li_{0.4}Zn_{0.2})Al_2O_4$ ceramics, presenting a relatively dense microstructure and uniform grain distribution when sintered at 1550 and 1600 °C, which match well with the high Qf values. However, the Qf values reduced due to the appearance of pores when the samples were sintered at 1575 °C.

Therefore, the Qf value was affected by the relative density and covalency of A-site bond at 1525–1600 °C, and the Qf value was mainly affected by the relative density at 1500–1525 °C. Comparative analysis indicates that high-entropy $(Mg_{0.2}Co_{0.2}La_{0.2}Li_{0.2}Zn_{0.2})Al_2O_4$ ceramics exhibited a high Qf value (~63,300 GHz, see Fig. S8 in Supplementary Information). This may be attributed to its secondary phase $LaAlO_3$ that possessed a large Qf value (~65,000 GHz) [52]. Compared to $MgAl_2O_4$ ceramics (~42,000 GHz), high-entropy $(Mg_{0.2}Co_{0.2}Ni_{0.2}Li_{0.4}Zn_{0.2})Al_2O_4$ ceramics exhibited a higher Qf value (~58,200 GHz). Moreover, the Qf value of high-entropy $(Mg_{0.2}Co_{0.2}Ni_{0.2}Li_{0.4}Zn_{0.2})Al_2O_4$ ceramics was higher than that of $(Mg_{0.25}Co_{0.25}Ni_{0.25}Zn_{0.25})Al_2O_4$ ceramics (see Fig. S9 in Supplementary Information). The relatively high Qf values are probably due to the high-configuration entropy and/or the property of Li^+ ions to act as acceptor dopant.

Fig. 7(d) shows the τ_f values of the high-entropy $(Mg_{0.2}Co_{0.2}Ni_{0.2}Li_{0.4}Zn_{0.2})Al_2O_4$ ceramics sintered at 1500–1600 °C. It is well known that the τ_f value is related to the coefficient of thermal expansion (α_L) and the temperature coefficient of the dielectric constant (τ_ε), thus the τ_f value could be calculated by using the following equation:

$$\tau_f = -\frac{1}{2}\tau_\varepsilon - \alpha_L \tag{9}$$

In general, α_L is the linear expansion coefficient and $\alpha_L = 10$ ppm/°C. Therefore, the τ_f value is mainly dependent on the τ_ε value. According to the Clausius–Mosotti equation, τ_ε could be calculated by using the following equation [58]:

$$\tau_\varepsilon = \frac{1}{\varepsilon}\left(\frac{\partial \varepsilon}{\partial T}\right) = \frac{(\varepsilon-1)(\varepsilon-2)}{\varepsilon}(A+B+C) \tag{10}$$

$$A = -\frac{1}{3V}\left(\frac{\partial V}{\partial T}\right)_p, B = \frac{1}{3V}\left(\frac{\partial \alpha_m}{\partial T}\right)_T\left(\frac{\partial V}{\partial T}\right)_p, C = \frac{1}{3\alpha_m}\left(\frac{\partial \alpha_m}{\partial T}\right)_V \tag{11}$$

where α_m and V represent the polarizability and volume, respectively. The parameters A and B are related to the volume expansion. They exhibit nearly equal magnitude and opposite signs. Therefore, the sum of A and B is approximately zero. Thus, the effect of A and B on τ_ε is negligible [59]; consequently, the τ_ε value is mainly determined by C. The term C relates to the restoring force associated with the structural parameters of the sample, such as bond strength [60]. In this study, the A-site bond strength (S_{A-O}) of high-entropy $(Mg_{0.2}Co_{0.2}Ni_{0.2}Li_{0.4}Zn_{0.2})Al_2O_4$ ceramics was calculated by using the following equation [56]:

$$S = \sum s_o\left(\frac{R_i}{R_o}\right)^{-N} \tag{12}$$

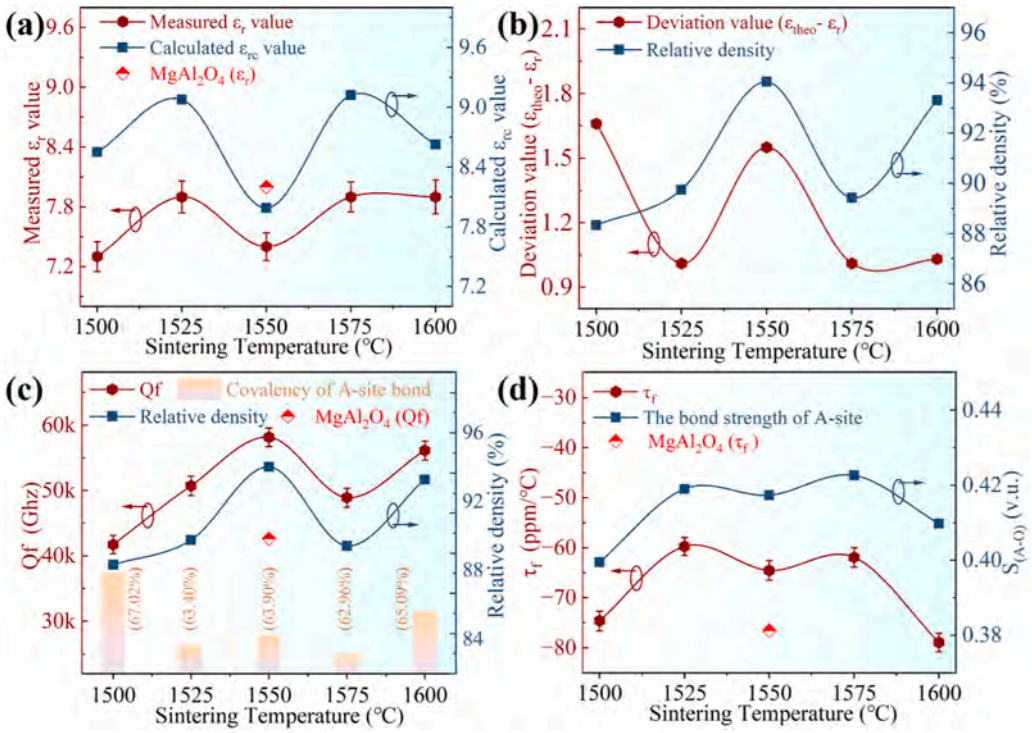

Fig. 7. Microwave dielectric properties of high-entropy $(Mg_{0.2}Co_{0.2}Ni_{0.2}Li_{0.4}Zn_{0.2})Al_2O_4$ ceramics. (a) The ε_r and ε_{rc} values; (b) The deviation value between ε_{theo} and ε_r value and relative density; (c) The Qf values, relative density and covalency of A-site bond; (d) The τ_f values and bond strength of A-site.

where R_i denotes the bond length from the refinement, and the empirical constants s_0, R_0, and N were obtained from the literature study. The s_0, R_0, and N values of Mg are 0.333, 2.076, and 5.2, respectively (see Table S7 in Supplementary Information).

In general, the decrease of the bond strength indicates that the restoring force of recovering the tilted oxygen polyhedron decreases [61]. Therefore, the reduction of A-site bond strength results in a larger degree of distortion of oxygen polyhedron, which is reflected in the decline in τ_f value. Besides, the expected tendency is observed in Fig. 7 (d), with the change in the sintering temperature from 1500 to 1600 °C. Moreover, the variation trend of the τ_f values of high-entropy $(Mg_{0.2}Co_{0.2}La_{0.2}Li_{0.2}Zn_{0.2})Al_2O_4$ ceramics is similar to that of the bond strength of A-site (see Fig. S10 in Supplementary Information). However, the τ_f values of high-entropy $(Mg_{0.2}Co_{0.2}La_{0.2}Li_{0.2}Zn_{0.2})Al_2O_4$ ceramics exhibited an opposite trend to the bond strength of A-site due to the reduction in the content of the secondary phase ($LaAlO_3$) at 1550–1600 °C. Moreover, compared to $MgAl_2O_4$ ceramics (–78 ppm/°C), high-entropy $(Mg_{0.2}Co_{0.2}Ni_{0.2}Li_{0.4}Zn_{0.2})Al_2O_4$ ceramics exhibited a large τ_f value (–64 ppm/°C).

4. Conclusions

In this study, high-entropy spinel-type $(Mg_{0.2}Co_{0.2}Ni_{0.2}Li_{0.4}Zn_{0.2})Al_2O_4$ ceramics were prepared successfully by solid-state reaction method. The high-configuration entropy and low average atomic-size difference were found to be beneficial to form a single-phase high-entropy ceramic structure. The raw materials gradually formed spinel aluminates from 700 to 1400 °C and ultimately formed single-phase high-entropy $(Mg_{0.2}Co_{0.2}Ni_{0.2}Li_{0.4}Zn_{0.2})Al_2O_4$ ceramics after calcination at 1400 °C for 4 h. Compared with $MgAl_2O_4$ ceramics, high-entropy $(Mg_{0.2}Co_{0.2}Ni_{0.2}Li_{0.4}Zn_{0.2})Al_2O_4$ ceramics exhibited enhanced microwave dielectric properties (ε_r = 7.4, Qf = 58,200 GHz, and τ_f = –64 ppm/°C). Furthermore, the ε_r, Qf, and τ_f are mainly dominated by dielectric polarizability, relative density, covalency of A-site bond, and bond strength of A-site in high-entropy $(Mg_{0.2}Co_{0.2}Ni_{0.2}Li_{0.4}Zn_{0.2})Al_2O_4$ ceramics. Excellent microwave dielectric properties make high-entropy $(Mg_{0.2}Co_{0.2}Ni_{0.2}Li_{0.4}Zn_{0.2})Al_2O_4$ ceramics an ideal candidate for applications in millimeter-wave communication.

Declaration of Competing Interest

The authors declare that they have no known competing financial interests or personal relationships that could have appeared to influence the work reported in this paper.

Acknowledgements

This research was funded by the Sichuan Science and Technology Program (No. 2023YFQ0082). Guangdong Provincial Key Laboratory of Electronic Functional Materials and Devices, grant number EFMD2022005Z. State Key Laboratory of Advanced Technologies for Comprehensive Utilization of Platinum Metals under Grant No. SKL-SPM-202021.

Appendix A. Supporting information

Supplementary data associated with this article can be found in the online version at doi:10.1016/j.jeurceramsoc.2023.09.017.

References

[1] B. Liu, L. Li, K.X. Song, M.M. Mao, Z. Lu, G. Wang, L. Li, D. Wang, D. Zhou, A. Feteira, I.M. Reaney, Enhancement of densification and microwave dielectric properties in LiF ceramics via a cold sintering and post-annealing process, J. Eur. Ceram. Soc. 41 (2021) 1726–1729, https://doi.org/10.1016/j.jeurceramsoc.2020.09.073.

[2] B. Liu, K. Sha, Y.Q. Jia, Y.H. Huang, C.C. Hu, L. Li, D.W. Wang, D. Zhou, K.X. Song, High quality factor cold sintered LiF ceramics for microstrip patch antenna applications, J. Eur. Ceram. Soc. 41 (2021) 4835–4840, https://doi.org/10.1016/j.jeurceramsoc.2021.03.052.

[3] B. Liu, K. Sha, M.F. Zhou, K.X. Song, Y.H. Huang, C.C. Hu, Novel low-ε_r MGa_2O_4 (M = Ca, Sr) microwave dielectric ceramics for 5 G antenna applications at the Sub-6 GHz, Band., J. Eur. Ceram. Soc. 41 (2021) 5170–5175, https://doi.org/10.1016/j.jeurceramsoc.2021.04.033.

[4] X. Zhang, Z. Jiang, B. Tang, Z. Fang, Z. Xiong, H. Li, C. Yuan, S. Zhang, A new series of low-loss multicomponent oxide microwave dielectrics with a rock salt structure: Li_5MgABO_8 (A=Ti, Sn; B=Nb, Ta, Ceram. Int. 46 (2020) 10332–10340, https://doi.org/10.1016/j.ceramint.2020.01.029.

[5] Y. Lai, Y. Zeng, J. Han, X. Liang, X. Zhong, M. Liu, B. Duo, H. Su, Structure dependence of microwave dielectric properties in $Zn_{2-x}SiO_{4-x}$-xCuO ceramics, J. Eur. Ceram. Soc. 41 (2021) 2602–2609, https://doi.org/10.1016/j.jeurceramsoc.2020.12.013.

[6] X.K. Lan, J. Li, Z.Y. Zou, M.Q. Xie, G.F. Fan, W.Z. Lu, W. Lei, Improved sinterability and microwave dielectric properties of $[Zn_{0.5}Ti_{0.5}]^{3+}$-doped $ZnAl_2O_4$ spinel solid solution, J. Am. Ceram. Soc. 102 (2019) 5952–5957, https://doi.org/10.1111/jace.16453.

[7] Y. Li, R. Fu, M.Y. Gao, M. Chen, R. Peng, Y. Lu, Improved $Zn_{0.9}Mg_{0.1}Al_2O_4$ microwave dielectric ceramics with high thermal conductivity, J. Electron. Mater. 50 (2021) 3372–3379, https://doi.org/10.1007/s11664-021-08829-4.

[8] Y. Lai, X. Tang, X. Huang, H. Zhang, X. Liang, J. Li, H. Su, Phase composition, crystal structure and microwave dielectric properties of $Mg_{2-x}Cu_xSiO_4$ ceramics, J. Eur. Ceram. Soc. 38 (2018) 1508–1516, https://doi.org/10.1016/j.jeurceramsoc.2017.10.035.

[9] Y. Lai, X. Tang, H. Zhang, X. Liang, X. Huang, Y. Li, H. Su, Correlation between structure and microwave dielectric properties of low-temperature-fired Mg_2SiO_4 ceramics, Mater. Res. Bull. 99 (2018) 496–502, https://doi.org/10.1016/j.materresbull.2017.11.036.

[10] W. Lou, K. Song, F. Hussain, B. Liu, H.B. Bafrooei, H. Lin, W. Su, F. Shi, D. Wang, Bond characteristics and microwave dielectric properties of $(Li_{0.5}Ga_{0.5})^{2+}$ doped $Mg_2Al_4Si_5O_{18}$ ceramics, Ceram. Int 46 (2020) 28631–28638, https://doi.org/10.1016/j.ceramint.2020.08.022.

[11] K. Du, X.Q. Song, Z.Y. Zou, J. Fan, W.Z. Lu, W. Lei, Improved microwave dielectric properties of novel low-permittivity Sn-doped $Ca_2HfSi_4O_{12}$ ceramics, Mater. Res. Bull. 129 (2020), 110887, https://doi.org/10.1016/j.materresbull.2020.110887.

[12] S. Takahashi, A. Kan, H. Ogawa, Microwave dielectric properties and crystal structures of spinel-structured $MgAl_2O_4$ ceramics synthesized by a molten-salt method, J. Eur. Ceram. Soc. 37 (2017) 1001–1006, https://doi.org/10.1016/j.jeurceramsoc.2016.10.018.

[13] H. Yu, T. Luo, L. He, J. Liu, Effect of ZnO on Mg_2TiO_4–$MgTiO_3$–$CaTiO_3$ microwave dielectric ceramics prepared by reaction sintering route, Adv. Appl. Ceram. 118 (2019) 98–105, https://doi.org/10.1080/17436753.2018.1525934.

[14] X. Yang, Y. Lai, Y. Zeng, F. Yang, F. Huang, B. Li, F. Wang, C. Wu, H. Su, Spinel-type solid solution ceramic $MgAl_2O_4$-Mg_2TiO_4 with excellent microwave dielectric properties, J. Alloys Compd. 898 (2022), 162905, https://doi.org/10.1016/j.jallcom.2021.162905.

[15] T. Qin, C. Zhong, Y. Qin, B. Tang, S. Zhang, The structure evolution and microwave dielectric properties of $MgAl_{2-x}(Mg_{0.5}Ti_{0.5})_xO_4$ solid solutions, Ceram. Int. 46 (2020) 19046–19051, https://doi.org/10.1016/j.ceramint.2020.04.236.

[16] J.W. Yeh, Recent progress in high-entropy alloys, Ann. Chim. Sci. Des. Mater. 31 (2006) 633–648, https://doi.org/10.3166/acsm.31.633-648.

[17] C.M. Rost, E. Sachet, T. Borman, A. Moballegh, E.C. Dickey, D. Hou, J.L. Jones, S. Curtarolo, J.P. Maria, Entropy-stabilized oxides, Nat. Commun. 6 (2015), https://doi.org/10.1038/ncomms9485.

[18] R.Z. Zhang, M.J. Reece, Review of high entropy ceramics: design, synthesis, structure and properties, J. Mater. Chem. A. 7 (2019) 22148–22162, https://doi.org/10.1039/c9ta05698j.

[19] H. Xiang, L. Yao, J. Chen, A. Yang, H. Yang, L. Fang, Microwave dielectric high-entropy ceramic $Li(Gd_{0.2}Ho_{0.2}Er_{0.2}Yb_{0.2}Lu_{0.2})GeO_4$ with stable temperature coefficient for low-temperature cofired ceramic technologies, J. Mater. Sci. Technol. 93 (2021) 28–32, https://doi.org/10.1016/j.jmst.2021.03.057.

[20] S. Zhou, Y. Pu, Q. Zhang, R. Shi, X. Guo, W. Wang, J. Ji, T. Wei, T. Ouyang, Microstructure and dielectric properties of high entropy Ba$(Zr_{0.2}Ti_{0.2}Sn_{0.2}Hf_{0.2}Me_{0.2})O_3$ perovskite oxides, Ceram. Int. 46 (2020) 7430–7437, https://doi.org/10.1016/j.ceramint.2019.11.239.

[21] D. Bérardan, S. Franger, D. Dragoe, A.K. Meena, N. Dragoe, Colossal dielectric constant in high entropy oxides, Phys. Status Solidi - Rapid Res. Lett. 10 (2016) 328–333, https://doi.org/10.1002/pssr.201600043.

[22] J. Rodríguez-Carvajal, Recent advances in magnetic structure determination by neutron powder diffraction, Phys. B Phys. Condens. Matter 192 (1993) 55–69, https://doi.org/10.1016/0921-4526(93)90108-I.

[23] S. Akrami, P. Edalati, M. Fuji, K. Edalati, High-entropy ceramics: Review of principles, production and applications, Mater. Sci. Eng. R. Rep. 146 (2021), 100644, https://doi.org/10.1016/j.mser.2021.100644.

[24] J. Gild, Y. Zhang, T. Harrington, S. Jiang, T. Hu, M.C. Quinn, W.M. Mellor, N. Zhou, K. Vecchio, J. Luo, High-entropy metal diborides: a new class of high-entropy materials and a new type of ultrahigh temperature ceramics, Sci. Rep. 6 (2016) 2–11, https://doi.org/10.1038/srep37946.

[25] P. Zhang, Z. Lou, M. Qin, J. Xu, J. Zhu, Z. Shi, Q. Chen, M.J. Reece, H. Yan, F. Gao, High-entropy $(Ca_{0.2}Sr_{0.2}Ba_{0.2}La_{0.2}Pb_{0.2})TiO_3$ perovskite ceramics with A-site short-range disorder for thermoelectric applications, J. Mater. Sci. Technol. 97 (2022) 182–189, https://doi.org/10.1016/j.jmst.2021.05.016.

[26] T. Qin, C. Zhong, Y. Shang, L. Cao, M. Wang, B. Tang, S. Zhang, Effects of LiF on crystal structure, cation distributions and microwave dielectric properties of $MgAl_2O_4$, J. Alloys Compd. 886 (2021), 161278, https://doi.org/10.1016/j.jallcom.2021.161278.

[27] E.S. Blaakmeer, F. Rosciano, E.R.H. Van Eck, Lithium doping of $MgAl_2O_4$ and $ZnAl_2O_4$ investigated by high-resolution solid state NMR, J. Phys. Chem. C. 119 (2015) 7565–7577, https://doi.org/10.1021/jp512304e.

[28] J. Li, M. Wei, L. Li, S. Tang, Citrate precursor synthesis of perovskite-type $NdAlO_3$ as a microwave dielectric material, J. Mater. Sci. Mater. Electron 31 (2020) 15352–15360, https://doi.org/10.1007/s10854-020-04099-8.

[29] C. Xin, M. Hu, K. Wang, X. Wang, Significant enhancement of photocatalytic reduction of CO_2 with H_2O over ZnO by the formation of basic zinc carbonate, Langmuir 33 (2017) 6667–6676, https://doi.org/10.1021/acs.langmuir.7b00620.

[30] M. JAVANMARDI, R. EMADI, H. ASHRAFI, Synthesis of nickel aluminate nanoceramic compound from aluminum and nickel carbonate by mechanical alloying with subsequent annealing, Trans. Nonferrous Met. Soc. China (Engl. Ed.) 26 (2016) 2910–2915, https://doi.org/10.1016/S1003-6326(16)64420-5.

[31] Z. Ouyang, P. Wen, Y. Chen, L. Ye, Study on thermodynamic equilibrium and character inheritance of cobalt carbonate decomposition, Vacuum 179 (2020), 109559, https://doi.org/10.1016/j.vacuum.2020.109559.

[32] M.Y. Nassar, Size-controlled synthesis of $CoCO_3$ and Co_3O_4 nanoparticles by free-surfactant hydrothermal method, Mater. Lett. 94 (2013) 112–115, https://doi.org/10.1016/j.matlet.2012.12.039.

[33] L.D. Shi L, T. Qu, Process of thermal decomposition of lithium carbonate, Mater. Process. Fundam. 2020 (2020) 107–116, https://doi.org/10.1007/978-3-030-36556-1_10.

[34] A.N. Timoshevskii, M.G. Ktalkherman, V.A. Emel'Kin, B.A. Pozdnyakov, A. P. Zamyatin, High-temperature decomposition of lithium carbonate at atmospheric pressure, High. Temp. 46 (2008) 414–421, https://doi.org/10.1134/S0018151×0803019X.

[35] Y. Duan, D.C. Sorescu, Density functional theory studies of the structural, electronic, and phonon properties of Li_2O and Li_2CO_3: application to CO_2 capture reaction, Phys. Rev. B - Condens. Matter Mater. Phys. 79 (2009) 1–18, https://doi.org/10.1103/PhysRevB.79.014301.

[36] V. Kaplan, E. Wachtel, K. Gartsman, Y. Feldman, I. Lubomirsky, Conversion of CO_2 to CO by electrolysis of molten lithium carbonate, J. Electrochem. Soc. 157 (2010) B552, https://doi.org/10.1149/1.3308596.

[37] X.M. Wang, X. Bai, H.Y. Duan, Z.X. Shi, J. Sun, S.G. Lu, S.T. Huang, Preparation of Al-doped ZnO sputter target by hot pressing, Trans. Nonferrous Met. Soc. China (Engl. Ed.) 21 (2011) 1550–1556, https://doi.org/10.1016/S1003-6326(11)60895-9.

[38] A. Mallick, A. Kole, T. Ghosh, P. Chaudhuri, D. Basak, Zinc aluminate spinel impurity phase in Al doped ZnO ceramic target and pulsed laser ablated films: curse or blessing, Sol. Energy 108 (2014) 80–87, https://doi.org/10.1016/j.solener.2014.05.049.

[39] N.J. van der Laag, M.D. Snel, P.C.M.M. Magusin, G. de With, Structural, elastic, thermophysical and dielectric properties of zinc aluminate ($ZnAl_2O_4$), J. Eur. Ceram. Soc. 24 (2004) 2417–2424, https://doi.org/10.1016/j.jeurceramsoc.2003.06.001.

[40] H.R. Zargar, M.R. Bayati, H.R. Rezaie, F. Golestani-Fard, R. Molaei, S. Zanganeh, A. Kajbafvala, Influence of nano boehmite on solid state reaction of alumina and magnesia, J. Alloys Compd. 507 (2010) 443–447, https://doi.org/10.1016/j.jallcom.2010.07.186.

[41] E.Y. Sako, M.A.L. Braulio, D.H. Milanez, P.O. Brant, V.C. Pandolfelli, Microsilica role in the CA_6 formation in cement-bonded spinel refractory castables, J. Mater. Process. Technol. 209 (2009) 5552–5557, https://doi.org/10.1016/j.jmatprotec.2009.05.013.

[42] S. Mukhopadhyay, P.K.Das Poddar, Effect of preformed and in situ spinels on microstructure and properties of a low cement refractory castable, Ceram. Int. 30 (2004) 369–380, https://doi.org/10.1016/S0272-8842(03)00117-2.

[43] K. Suzuki, Y. Kuroki, T. Okamoto, M. Takata, Cathodoluminescence of single phase $ZnAl_2O_4$ and diffusion layer synthesized by coupling of ZnO and α-Al_2O_3, Key Eng. Mater. 350 (2007) 233–236, https://doi.org/10.4028/www.scientific.net/kem.350.233.

[44] X.Y. Chen, J.H. Li, Z.H. Sun, X. Fang, Z.P. Wei, F. Fang, X.Y. Chu, S. Li, X.H. Wang, The formation and acceptor related emission behavior of ZnO/$ZnAl_2O_4$ core-shell structures, J. Alloys Compd. 571 (2013) 114–117, https://doi.org/10.1016/j.jallcom.2013.03.198.

[45] S. Sommer, E.D. Bøjesen, A.B. Blichfeld, B.B. Iversen, Tailoring band gap and thermal diffusivity of nanostructured phase-pure $ZnAl_2O_4$ by direct spark plasma sintering synthesis, J. Solid State Chem. 256 (2017) 45–52, https://doi.org/10.1016/j.jssc.2017.08.023.

[46] R.D. Shannon, Dielectric polarizabilities of ions in oxides and fluorides, J. Appl. Phys. 73 (1993) 348–366, https://doi.org/10.1063/1.353856.

[47] S.J. Penn, N.M.N. Alford, A. Templeton, X. Wang, M. Xu, M. Reece, K. Schrapel, Effect of porosity and grain size on the microwave dielectric properties of sintered alumina, J. Am. Ceram. Soc. 80 (1997) 1885–1888, https://doi.org/10.1111/j.1151-2916.1997.tb03066.x.

[48] J. Li, Y. Han, T. Qiu, C. Jin, Effect of bond valence on microwave dielectric properties of (1-x)$CaTiO_3$-$x(Li_{0.5}La_{0.5})TiO_3$ ceramics, Mater. Res. Bull. 47 (2012) 2375–2379, https://doi.org/10.1016/j.materresbull.2012.05.024.

[49] K.H. Yoon, E.S. Kim, J.S. Jeon, Understanding the microwave dielectric properties of $(Pb_{0.45}Ca_{0.55})[Fe_{0.5}(Nb_{1-x}Ta_x)_{0.5}]O_3$ ceramics via the bond valence, J. Eur. Ceram. Soc. 23 (2003) 2391–2396, https://doi.org/10.1016/S0955-2219(03)00187-0.

[50] C. Li, J. Hou, Z. Ye, R. Muhammad, A. Li, M. Ma, G. Wu, K. Song, T. Zhou, M. Mao, B. Liu, H.B. Bafrooei, E. Taheri-nassaj, S. Luo, F. Shi, S. Sun, D. Wang, Lattice occupying sites and microwave dielectric properties of Mg^{2+}–Si^{4+} co-doped $Mg_xY_{3-x}Al_{5-x}Si_xO_{12}$ garnet typed ceramics, J. Mater. Sci. Mater. Electron. 33 (2022) 2116–2124, https://doi.org/10.1007/s10854-021-07417-w.

[51] X. Zhu, F. Kong, X. Ma, Sintering behavior and properties of $MgTiO_3$/CaO-B_2O_3-SiO_2 ceramic composites for LTCC applications, Ceram. Int. 45 (2019) 1940–1945, https://doi.org/10.1016/j.ceramint.2018.10.086.

[52] H.J.J. Dong-Gee Lim, B. Ho Kim, T.-G. Kim, Microwave dielectrics properties of the (1-x)$LaAlO_3$-$xTiO_2$ system, Appl. Phys. A. 34 (1999) 1577–1582, https://doi.org/10.1016/S0025-5408(99)00186-5.

[53] Y. Lai, H. Su, G. Wang, X. Tang, X. Huang, X. Liang, H. Zhang, Y. Li, K. Huang, X. R. Wang, Low-temperature sintering of microwave ceramics with high Qf values through LiF, Addit. J. Am. Ceram. Soc. 102 (2019) 1893–1903, https://doi.org/10.1111/jace.16086.

[54] H.J. Jo, E.S. Kim, Effects of structural characteristics on microwave dielectric properties of $MgTi_{1-x}(Mg_{1/3}B_{2/3})_xO_3$ (B = Nb, Ta), J. Eur. Ceram. Soc. 36 (2016) 1399–1405, https://doi.org/10.1016/j.jeurceramsoc.2015.12.033.

[55] A. Kan, H. Ogawa, H. Ohsato, Synthesis and crystal structure-microwave dielectric property relations in Sn-substituted $Ca_3(Zr_{1-x}Sn_x)Si_2O_9$ solid solutions with cuspidine structure, Japanese, J. Appl. Phys. Part 1 Regul. Pap. Short. Notes Rev. Pap. 46 (2007) 7108–7111, https://doi.org/10.1143/JJAP.46.7108.

[56] I.D. Brown, R.D. Shannon, Empirical bond-strength–bond-length curves for oxides, Acta Crystallogr. Sect. A 29 (1973) 266–282, https://doi.org/10.1107/S0567739473000689.

[57] I.D. Brown, K.K. Wu, Empirical parameters for calculating cation–oxygen bond valences, Acta Crystallogr. Sect. B Struct. Crystallogr. Cryst. Chem. 32 (1976) 1957–1959, https://doi.org/10.1107/s0567740876006869.

[58] S.D. Rama Rao, S. Roopas Kiran, V.R.K. Murthy, Correlation between structural characteristics and microwave dielectric properties of scheelite $Ca_{1-x}Cd_xMoO_4$ solid solution, J. Am. Ceram. Soc. 95 (2012) 3532–3537, https://doi.org/10.1111/j.1551-2916.2012.05317.x.

[59] A.J. Bosman, E.E. Havinga, Temperature dependence of dielectric constants of cubic ionic compounds, Phys. Rev. 129 (1963) 1593–1600, https://doi.org/10.1103/PhysRev.129.1593.

[60] C. Li, S. Ding, Y. Zhang, H. Zhu, T. Song, Effects of Ni^{2+} substitution on the crystal structure, bond valence, and microwave dielectric properties of $BaAl_{2-2x}Ni_{2x}Si_2O_{8-x}$, Ceram. J. Eur. Ceram. Soc. 41 (2021) 2610–2616, https://doi.org/10.1016/j.jeurceramsoc.2020.12.011.

[61] Z. Xiong, C. Yang, B. Tang, Z. Fang, H. Chen, S. Zhang, Structure–property relationships of perovskite-structured $Ca_{0.61}Nd_{0.26}Ti_{1-x}(Cr_{0.5}Nb_{0.5})_xO_3$ ceramics, Ceram. Int. 44 (2018) 7384–7392, https://doi.org/10.1016/j.ceramint.2017.12.186.